SUPPLEMENTAL DATA

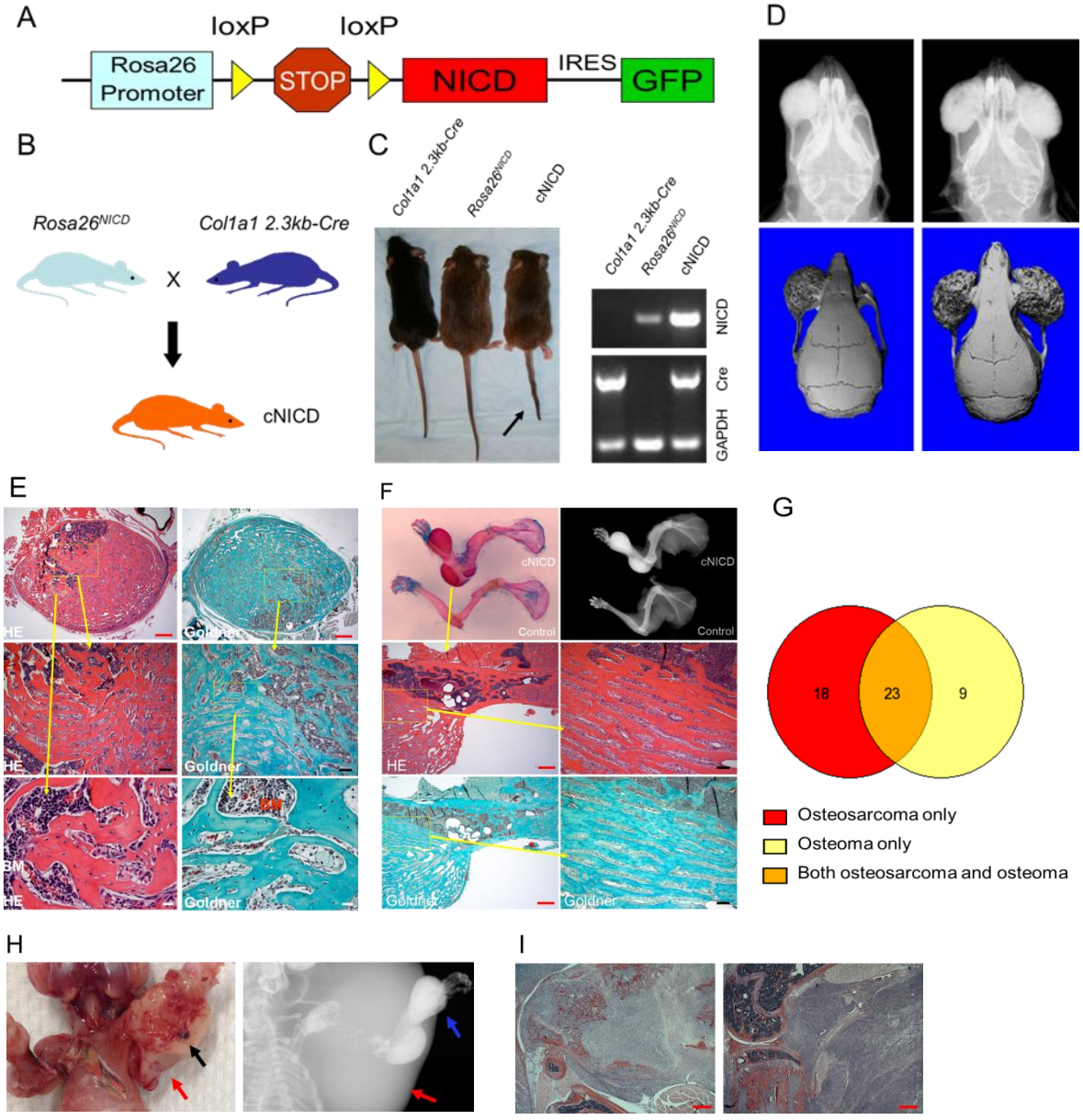

Figure S1. Related to Figure 1. Osteoblastic-specific expression of NICD *in vivo* leads to bone tumorigenesis. (A) The *Rosa26*^{NICD} allele comprises a loxP-flanked Neomycin resistance gene with a polyadenylation signal (STOP). This is followed by NICD cDNA and an encephalomyocarditis virus internal ribosomal entry site (IRES) fused to nuclear enhanced green fluorescent protein (GFP) cDNA. Presence of Cre leads to recombination between the two LoxP sites, thereby removing the STOP cassette, allowing transcription of NICD and GFP from the endogenous *Rosa26* promoter (Murtaugh et al., 2003). **(B)** Breeding scheme of the cNICD mice. **(C)** Living

image of 4-months-old cNICD mice and their littermates (left). Black arrow points to the kinky tail. Genotyping gel image (right) after PCR analysis of NICD, Cre, and GAPDH (as control) from mouse lines: *Col1a1 2.3kb-Cre* (lane 1), *Rosa26*^{NICD} (lane 2) and bi-allelic transgenic *Col1a1 2.3kb-Cre;Rosa26*^{NICD} (cNICD mice) (lane 3). (**D)** X-ray images (upper panels) and microCT scan (lower panels) show representative cNICD skulls bearing osteomas. Mono (left column) or bi-focal (right column) masses are seen in the skull. **(E)** Hematoxylin/eosin (H&E or HE)- (left column) and Goldner- (right column) stained histopathology of representative osteomas (top panels) from skulls showing woven bone and bone marrow (BM) at high magnification (middle and lower panels). **(F)** Photo of skeletal preparation of representative forelimbs from the cNICD and control mouse (top left), X-ray image of their forelimbs (top right), and H&E- (middle left, and a high magnification (middle right)) and Goldner- (bottom left, and a high magnification (bottom right)) stained histopathology of representative osteomas from the forelimb. (**G**) Venn diagram showing the number of mice bearing two types of bone tumors. The numbers refer to the mice having the indicated tumors. **(H)** Photo of a representative NOS tumor from forelimb displaying a white cut surface (red arrow) and a center area of hemorrhage and cystic degeneration (black arrow) (left). X-ray image of the same forelimb showing area of tumor mass (red arrow) and osteoma mass (blue arrow) (right) **(I)** H&E-stained histopathology of representative NOS from the distal femur (left) and the proximal tibia (right) showing destroyed cortical bone and medullary cavity filled with tumor cells. All red scale bars are 500 μm in length, the black bars are 100 μm and the white bar is 20 μm.

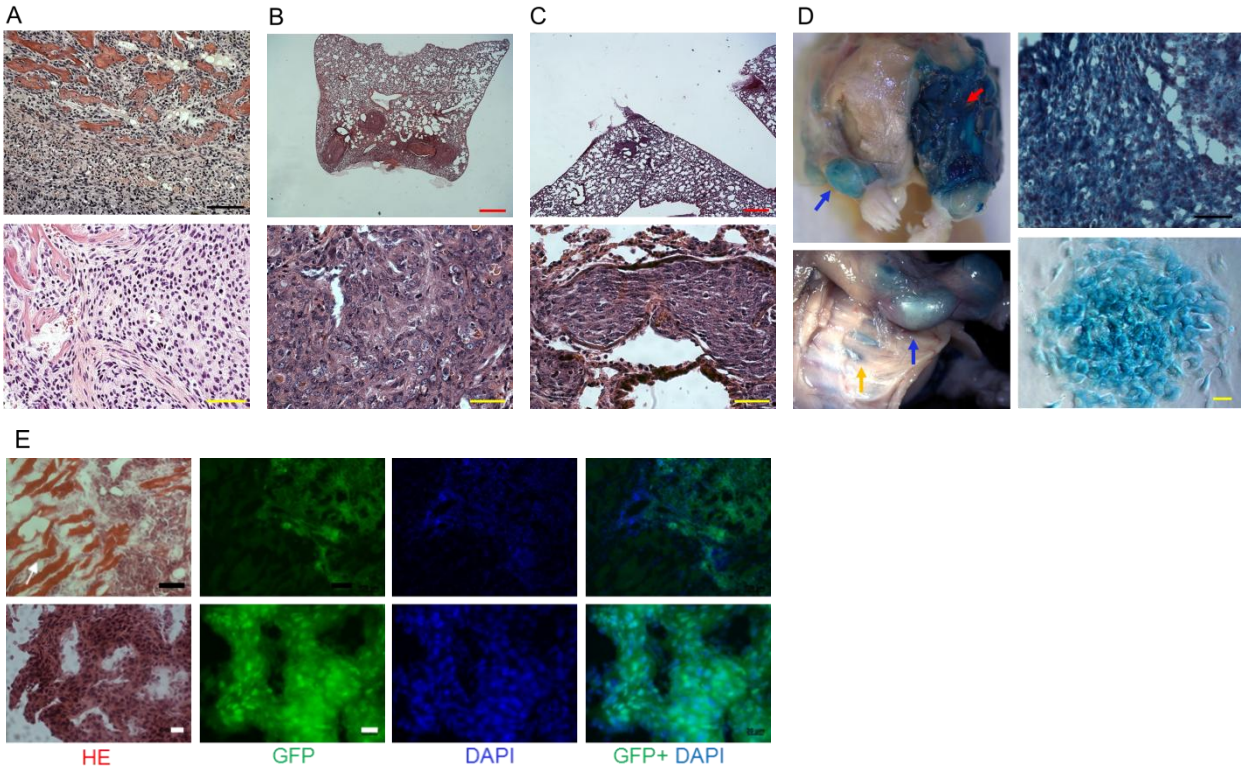

Figure S2. Related to Figure 2. Primary and metastatic NOS resemble human OS. **(A)** H&E-stained histopathology of representative primary NOS from either femur (top) or tibia (bottom) showing poorly differentiated or undifferentiated hypercellular lesions with areas of osteoid, and numerous spindle cells. **(B)** H&E-stained histopathology of a representative lung metastatic mass, which was first detected macroscopically showing multiple lesions in the lung (top) with high cellularity at high magnification (bottom). **(C)** H&E-stained histopathology of a representative lung metastatic mass, which was not detected macroscopically showing single lesions in the lung (top) with high cellularity at high magnification (bottom). **(D)** Photos of forelimbs with ventral body (top left) and a forelimb with lateral body (bottom right) from a tri-transgenic mouse (*Rosa26*^{NICD}; *Col1a1 2.3kb*-Cre; *Rosa26*^{LacZ}) with whole mount X-gal staining. LacZ activity (blue color) was detected in OS tumors (red arrow), osteomas (blue arrows), and ribs (orange arrow), and also in a cross section of primary OS (top right) and cultured cells derived from this tumor (bottom right). **(E)** H&E-stained histopathology (far left column) and immunofluorescent images of representative primary NOS showing tumor cells stained with GFP (green, middle left column), DAPI (blue, middle right column), and GFP merged with DAPI (far right column) at low (top panels) and high (bottom panels) magnification. White arrow points to adjacent muscle tissue. All red scale bars are 500 μm in length, the black bars are 100 μm, the yellow bars are 50 μm, and the white bars are 20 μm.

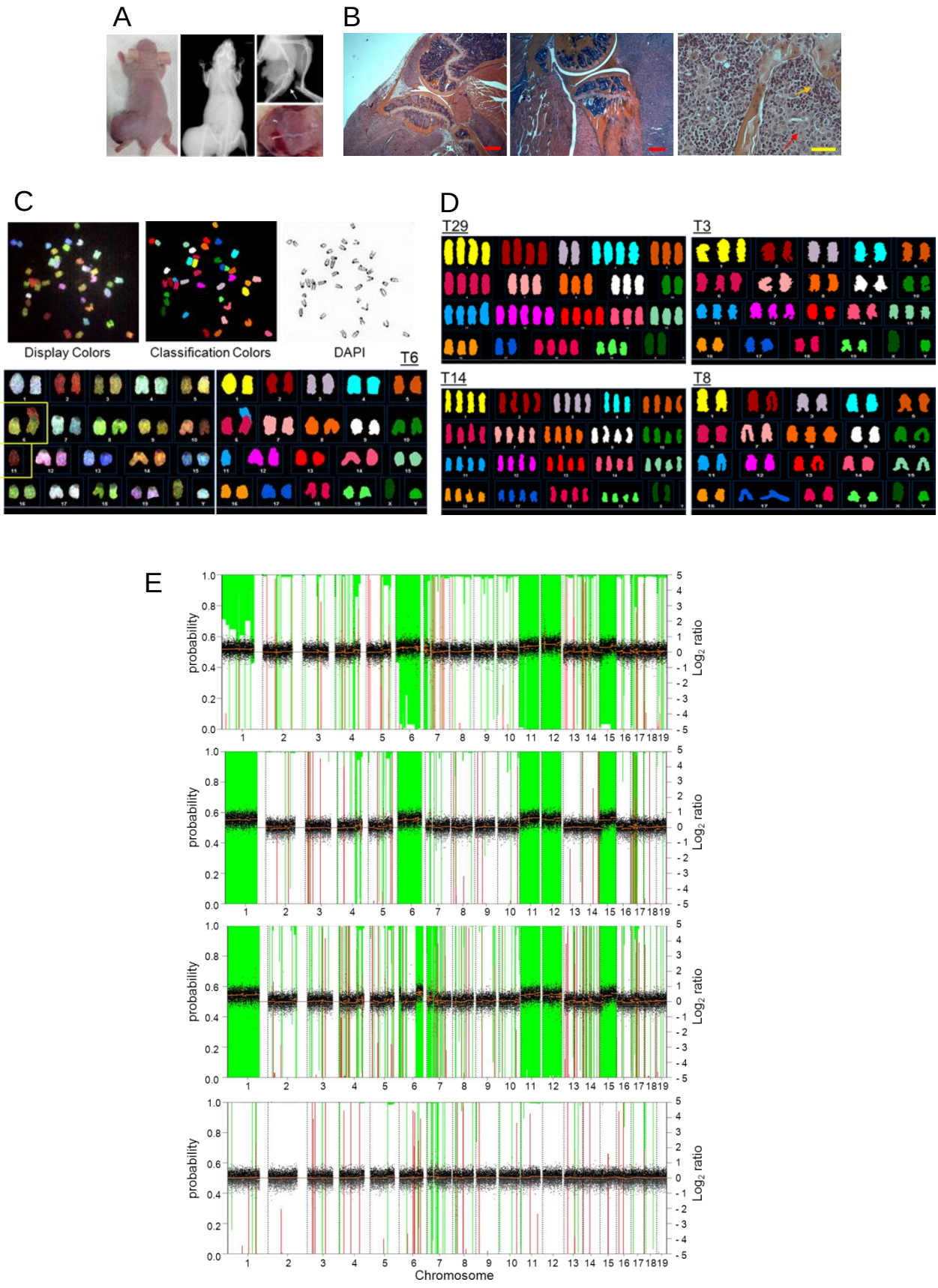
A
B
C
Display Colors
Classification Colors
DAPI
T6
D
T29
T3
T14
T8
E
probability
Log2 ratio
Chromosome

Figure S3. Related to Figure 3. NOS exhibits genomic instability. (A) Photo of a representative nude mouse (left) bearing a tumor after injection with the NOS-T14 cell line into the tibia and X-ray image of the same mouse (middle) showing a tumor (white arrow) in the tibia (top right). Bottom right photo shows the tumor after dissection. **(B)** H&E-stained histopathology of two representative transplanted tumors (left and middle) in tibia and a high magnification image (right) showing tumor cells (red arrow) mixed with marrow cells (yellow arrow). All red scale bars are 500 μm in length and the yellow bar is 50 μm. **(C)** Spectral karyotyping (SKY) evaluation of harvested cells from NOS-T6 cell line shows a Robertsonian translocation between chromosomes 6 and 11 (yellow frame, display colors in bottom left, and classification colors in bottom right). **(D)** SKY evaluation of NOS cells showing aneuploidy, including a nearly tetraploid karyotype in NOS T29 and T14 and trisomy in NOS T3 and T8. **(E)** Genome level log2 ratio plots from NOS T14 (top), NOS T1 (middle top), NOS T6 (middle bottom), and NOS T29 (bottom). CNV-seq from shotgun sequence data from tumor and non-tumor control demonstrates similarities and differences between different tumors. The normalized log2-ratios are plotted with the scale on the right axis. Vertical bars indicate loss and gain probabilities according to the left axis. The plot is comprised of log2-ratio data points every 61bp (538k total), of which every 10th is visualized (10% resolution). Median absolute deviation (MAD) in each plot is about 0.28.

A

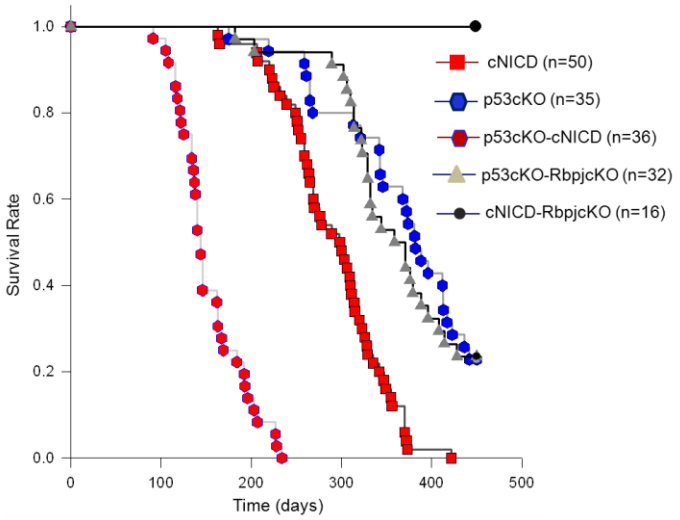

C

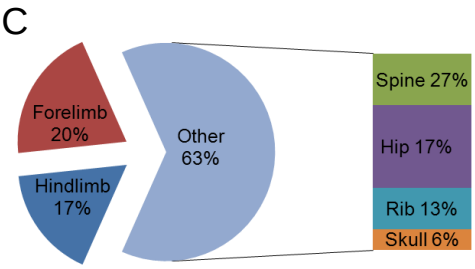

B

Comparisons	Unadjusted p Value	Significant
cNICD vs. p53cKO-cNICD	7.69E-23	Yes
p53cKO vs. p53cKO-cNICD	6.63E-19	Yes
p53cKO-cNICD vs. p53cKO-RbpjcK	2.62E-18	Yes
cNICD vs. cNICD-RbpjcKO	9.93E-12	Yes
p53cKO-cNICD vs. cNICD-RbpjcKO	3.82E-11	Yes
p53cKO vs. cNICD	4.93E-09	Yes
cNICD vs. p53cKO-RbpjcKO	0.000000324	Yes
p53cKO-RbpjcKO vs. cNICD-Rbpjc	0.00000326	Yes
p53cKO vs. cNICD-RbpjcKO	0.0000104	Yes
p53cKO vs. p53cKO-RbpjcKO	0.411	No

D

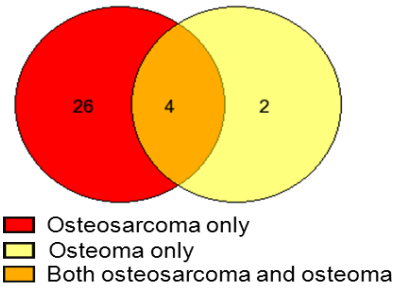

E

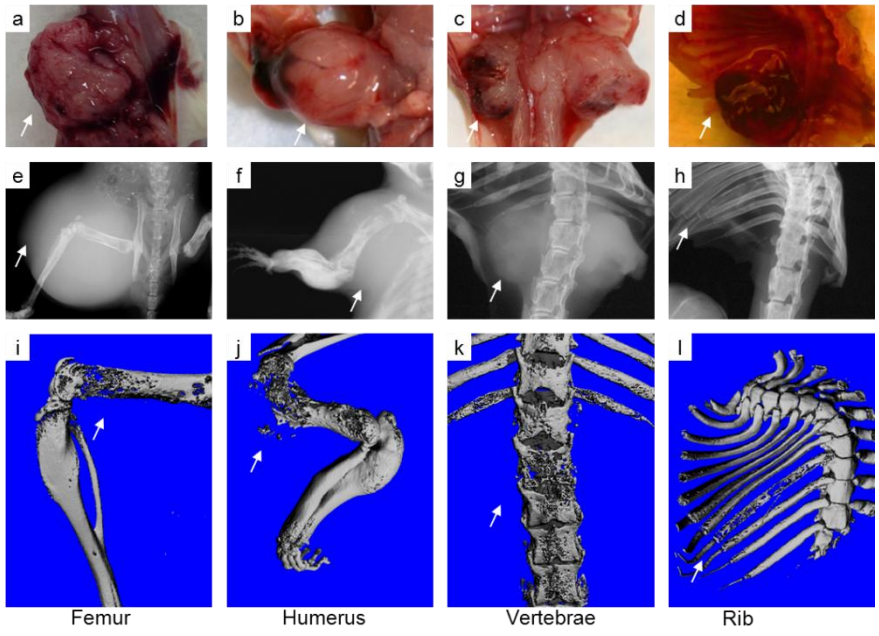

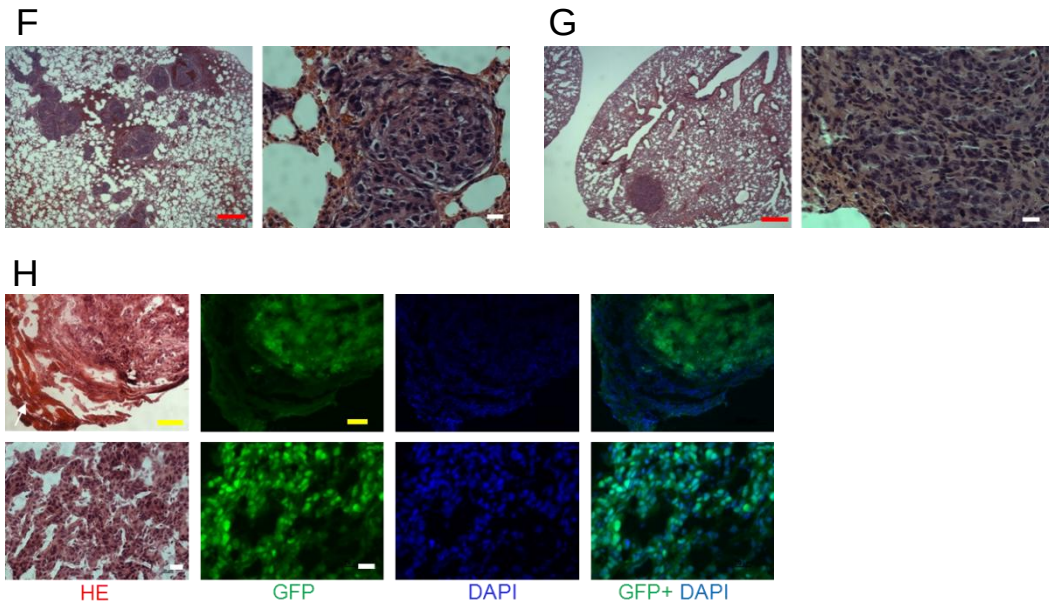

Figure S4, Related to Figure 4. Deletion of p53 in the cNICD (p53cKO-cNICD) mice significantly influences not only tumor initiation and progression but also a preference for tumor location. (A) Kaplan-Meier tumor-free survival plots of cNICD, p53cKO, p53cKO-cNICD, p53cKO-RbpjcKO and cNICD-RbpjcKO mice. n, number of mice. **(B)** Summary of results for comparisons between each cohort of mice used for statistical analysis with SigmaPlot. **(C)** Location and frequency of malignant bone tumors in the 30 of p53cKO-cNICD mice (the data did not include 4 mice from which we were unable to retrieve partial or whole carcasses) **(D)** Venn diagram showing the number of the p53cKO-cNICD mice bearing two types of bone tumors. The numbers refer to the mice having the indicated tumors. **(E)** Macroscopic analysis of tumors (a-d), X-ray imaging (e-h), and microscopic computed-tomography (micro-CT) scanning (i-l) confirmed a variety of bone sites. Representative tumors from p53cKO-cNICD mice are shown in the femur (a, e, i), humerus (b, f, j), vertebrae (c, g, k), and rib (d, h, l). White arrows point to the tumor mass. **(F)** H&E-stained histopathology of a representative lung metastatic mass showing multiple lesions in the lung (left) with high cellularity (right). **(G)** H&E-stained histopathology of a representative lung metastatic mass showing single lesions in the lung (left) with high cellularity (right). **(H)** H&E-stained histopathology (far left column) and immunofluorescent images of representative primary NOS showing tumor cells stained with GFP (green, middle left column), DAPI (blue, middle right column), and GFP merged with DAPI (far right column) at low (top panels) and high (bottom panels) magnification. White arrow points to adjacent muscle tissue. All red scale bars are 500 μm in length, the yellow bars are 100 μm, and the white bars are 20 μm.

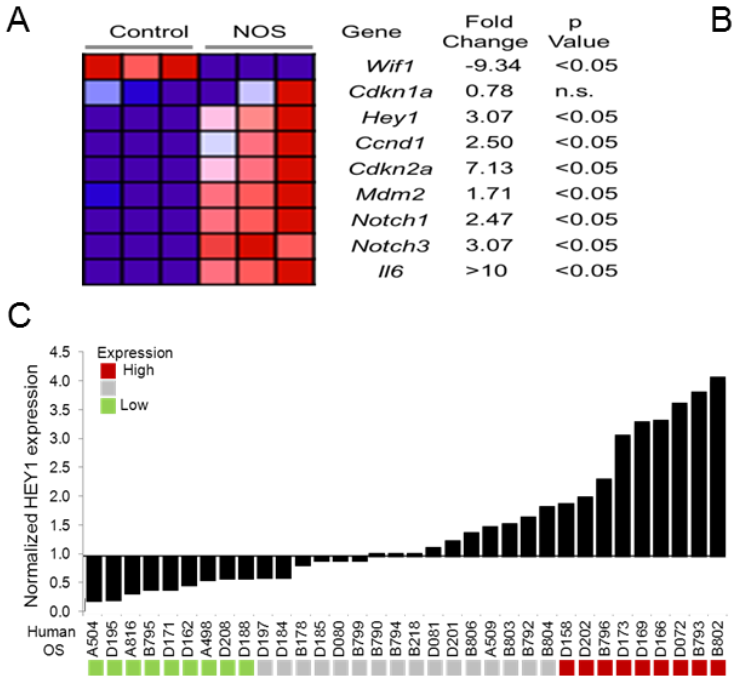

B

Human Region	NOS primary malignant tumors		
	NOM p val	FDR q val	FWER p val
4Q27-33	0.001*	0.042*	0.048*
11P15	<0.001*	0.295	0.059
17P11-13	0.020*	0.398	0.615
8Q12-21.3	0.119	0.469	0.832
10Q26	0.159	0.479	0.914
7P22-13	0.162	0.579	0.975
22Q13	1.000	0.716	0.360
1Q11-13	0.351	0.748	0.999
12P13	0.462	0.761	1.000
1P11-13	0.515	0.775	1.000
7Q11-36	0.424	0.819	1.000
22Q11	0.647	0.889	0.304
6P25-23	0.423	0.902	1.000
19Q13	1.000	0.999	1.000
6P12.1	0.731	1.000	1.000
8Q23-24	0.962	1.000	1.000
22Q12	0.977	1.000	1.000
1Q21-22	0.988	1.000	1.000

Figure S5, Related to Figure 5. Expression analysis of candidate genes and evidence of Notch activation in human OS samples. (A) Heat map showing relative gene expression of tumors using RNA-seq data generated from three cNICD mice and control tissues from three wild-type mice. For each gene, the highest relative expression levels are shown in dark red and the lowest in dark blue. The right panel shows log2 fold change of RPKM and statistical significance in NOS relative to the control samples. n.s., not significant. **(B)** Summary of results generated from cytogenetic region enrichment analysis (CREA) for each of the indicated cytogenetic regions for NOS primary malignant tumors. Asterisks indicate statistical significance. **(C)** Analysis of *HEY1* expression by using published microarray data (Paoloni et al., 2009) generated from 34 human OS tumors, ranked low to high, with the lowest and highest 25% indicated.

Table S1, related to Figure 5. Significantly differentially expressed genes from Notch-initiated OS to Control. Provided as an Excel file.

Table S2, related to Figure 5. Significantly differentially expressed genes from p53-loss-initiated OS to Control. Provided as an Excel file.

Table S3, related to Figure 5. Pathways Analysis of significantly differentially expressed genes from Notch-initiated OS to Control. Provided as an Excel file.

Table S4, related to Figure 5. Pathways Analysis of significantly differentially expressed genes from p53-loss-initiated OS to Control. Provided as an Excel file.

SUPPLEMENTAL EXPERIMENTAL PROCEDURES

Generation of osteosarcoma cell lines and transplant assay

Osteosarcomas were dissected, minced with a scalpel blade, and filtered through a 70-μm cell strainer (BD Falcon) to remove clumps and plated in normal growth medium to generate the OS cell line as previously described (Ma et al., 2009). For transplant assays, 1–3 million tumor cells were injected s.c. or intra-tibially into nude mice. Moribund animals were euthanized, and tumors were collected for further experiments.

Skeletal preparation and histology

Staining of whole mount skeletal preparations with Alcian blue 8GX (Sigma Aldrich) and Alizarin red S (Sigma Aldrich) was performed as previously described (Tao et al., 2010). Littermates of control and mutant mice were sacrificed at different ages, and the whole skeletons were fixed in 10% neutral-buffered formalin overnight. Paraffin-embedded decalcified bones were sectioned at 6-μm thickness and stained with hematoxylin/eosin and Goldner's stains by using standard protocols. Limb skeletal preparations were photographed with a Nikon 5.0 megapixel digital camera mounted atop of a Nikon SMZ1500 dissecting scope. All microscope and camera settings were identical for the capture of the images. Digital image files were uploaded to an Axiovision software (Carl Zeiss Vision, Munchen-Hallbergmoos, Germany) connected to a Zeiss Axioplan 2 scope, and scale equivalency was achieved via transfer of stage micrometer calibration information. These procedures allowed for direct comparison of each image.

β-galactosidase staining

For whole mount staining of lungs and tumors for β-galactosidase activity, lungs or tumors with skeleton were harvested and fixed in 4% paraformaldehyde for from 20 min to a few hours at 4°C. They were washed and then stained by incubating in staining solution [1 mg/ml X-gal (5-bromo-4-chloro-3-indolyl-β-d-galactopyranoside), 40 mM citric acid/sodium phosphate (pH 6.0), 5 mM potassium ferrocyanide, 5 mM potassium ferricyanide, 150 mM NaCl, 2 mM magnesium chloride] a few hours at room temperature or overnight at 4°C. Following staining, lung or tumors were rinsed in

phosphate-buffered saline (PBS) and cleared in 30% sucrose. For cultures, plated cells were washed in PBS, fixed in 2% formaldehyde and 0.2% glutaraldehyde in PBS for 5 minutes, and then washed again in PBS and stained with X-gal solution.

Tumor and bone radiographic assessment

Mice bearing tumors were analyzed by whole-body X-ray using a Faxitron instrument (Kubtec XPERT 80 radiograph digital imaging system, Milford, CT, USA) according to the manufacturer's protocol to determine the sites of skeletal involvement. Before histologic processing, harvested bones bearing tumors were evaluated by micro-computed tomography (mCT-40, Scanco Medical AG, Bassersdorf, Switzerland) with a 55-kilovolt peak (kVp) source, as previously described (Tao et al., 2010). Skulls were scanned at a resolution of 12 μm with a slice increment of 10 μm. Images from each group were reconstructed at identical thresholds to allow three-dimensional structural rendering of the entire skull.

Tumor monitoring and histological analysis

The criteria for euthanasia (by CO_2 inhalation) were a total tumor burden of ~2 cm^3, presence of tumor ulceration/bleeding, signs of infection, respiratory distress, impaired mobility, and at least 20% reduction in body weight or general cachexia. All tissues were collected and whole skeletons with tumors were fixed overnight in 10% neutral-buffered formalin. Soft tissues were transferred into 70% ethanol and dehydrated with an ethanol solution series before embedding in paraffin for sectioning. Tissues containing bone were decalcified in 10% EDTA, 2.5% ammonium hydroxide, pH 7.2, for 4 days before sectioning. Paraffin-embedded decalcified bones were sectioned to a 6-μm thickness and the sections were stained with hematoxylin and eosin using standard protocols. All microscope and camera settings were identical for the capture of the images. Digital image files were uploaded to an Axiovision software (Carl Zeiss Vision, Munchen-Hallbergmoos, Germany) connected to a Zeiss Axioplan 2 scope, and scale equivalency was achieved via transfer of stage micrometer calibration information. These procedures allowed for direct comparison of each image.

Total RNA preparation and quantitative RT-PCR analysis

Total RNA extraction, first-strand cDNA synthesis, and real-time PCR were carried out as previously described (Engin et al., 2008; Tao et al., 2010). Briefly, RNA was extracted from either tumors or normal bone (n=3) of young mice with TRIzol reagent (Invitrogen, Camarillo, CA, USA). cDNAs were synthesized from extracted RNA with the Superscript III First Strand RT-PCR kit (Invitrogen), and real-time quantitative PCR amplifications were performed in a LightCycler (Roche, Indianapolis, IN, USA). The genes encoding GAPDH and beta-actin were used as reference genes in real-time PCR assays.

Cryosectioning and immunostaining

Collected tumors were immediately embedded in O.C.T compound (Tissue-Tek®). O.C.T blocks were preserved at -80°C and sectioned with a LEICA CM 3050S cryostat into 10-µm thickness slices. Standard protocols recommended by the antibody suppliers were followed for immunostaining (primary antibodies: GFP, 1:1000, A11122; secondary antibodies: goat-anti-rabbit antibody conjugated to Alexa Fluor®594, 1:600, Invitrogen). The negative control consisted of staining the cryosectioned slides with secondary antibody alone. All comparable samples were imaged with identical exposure times and conditions. The images were analyzed with the Zeiss Axiovision software.

Spectral karyotyping (SKY) analysis

SKY was performed as previously described (Lau et al., 2004). Briefly, low passage number (less than 5) osteosarcoma cell lines were harvested after overnight incubation with colcemid. Metaphase spreads of OS cells were hybridized using a mouse SkyPaint DNA Kit (Applied Spectral Imaging (ASI), Vista, CA, USA), following the manufacturer's instructions, overnight incubation with colcemid<foreign-keys><key,6-diamidino-2-phenylindole (DAPI). More than 7 metaphase cells were analyzed for each case. Images were acquired with a SD200 Spectra cube (ASI) mounted on a Zeiss Axioplan II microscope using a custom-designed optical filter (SKY-1) (Chroma Technology, Brattleboro, VT, USA) and analyzed using SKY View 2.1.1 software (ASI, Vista, CA, USA). The breakpoints on the SKY-painted chromosomes were determined by

comparison with the corresponding inverted-DAPI banding of the same chromosome and with the G-banded karyotype for each case. A breakpoint was considered recurrent if it was identified in 2 or more cases.

Kaplan–Meier survival analysis and statistical analyses

Kaplan–Meier survival plots were prepared using SigmaPlot (version 11.0, Systat Software, Inc., San Jose, CA, USA). Statistical analyses for all pairwise multiple comparisons were conducted using SigmaPlot software using the Holm-Sidak method. Statistical significance (p values) was computed with the Student's t-test.

RNA sequencing and data analysis

For RNA sequencing (RNA-seq), libraries were prepared according to the dUTP protocol (Parkhomchuk et al., 2009). Briefly, mRNAs were captured by oligodT magnetic beads and fragmented by using the RNA Fragmentation Reagents (Ambion, Austin, TX, USA). Random hexamer primers were used to generate the first strand cDNA. Second strand cDNA was then synthesized with dUTP and double strand cDNAs were used as the library template. The 5’ ends of DNA fragments were phosphorylated and a single adenine base was added to the 3’ ends using Klenow exo-nuclease. Y-shape Illumina adaptors were added to each end. One strand with dUTP was digested using UDG and the other one was used as the PCR template for 12 cycles. Size distribution of fragment was determined using an Agilent Bioanalyzer (Agilent Technologies, Santa Clara, CA, USA). Concentration of the library was measured by PicoGreen fluorescence assay. Sequencing was performed on an Illumina HiSeq 2000 instrument as 100 bp pair-end reads conducted at the Human Genome Sequencing Center at Baylor College of Medicine. Raw data were processed using a similar method to that previously described (Daines et al., 2011). Raw reads were mapped to mouse genome mm9 and splice junction sites with bowtie (v0.12.7) (Langmead et al., 2009) and Tophat (v2.0.0) (Trapnell et al., 2009) in the strand specific model when strand-specific library protocol is applied. The reference Mouse genome annotation file was downloaded from UCSC (http://genome.ucsc.edu/) with a timestamp of August 30, 2011. Read counts mapped to each gene were calculated by HTseq (http://www-

huber.embl.de/users/anders/ HTSeq/doc/overview.html) with the default model. Mapping rates for all samples were between 80% and 83%. After mapping and duplicate removal, 59% to 68% of the total number of reads remained. Fragments per kilobase of exon model per million fragments mapped (FPKM) values were calculated using Cufflinks (version 2.1.1, http://cufflinks.cbcb.umd.edu) (Trapnell et al., 2012). Raw sequencing data from RNA-sequencing of Notch-induced tumors have been deposited into NCBI SRA database (accession number: SRP036832).

Differential expression and functional annotation analysis

Differential expression was analyzed with R (v2.14.0, http://www.R-project.org) (Ihaka and Gentleman, 1996) and Bioconductor (release 2.10) (Gentleman et al., 2004) with the R package DESeq (v1.6.0) (Anders and Huber, 2010). In cases of absence of biological replicates, the method of "blind" with sharing mode of "fit-only" was used to estimate dispersions in DESeq. Genes with an adjusted p value below 0.05 were considered as being differentially expressed. FPKMs resulting from three cohorts of samples were analyzed and the fold change was determined by comparing Notch-induced osteosarcoma (OS) to bone control tissues. RNA-seq data from the p53-induced OS data have been previously published (Straessler et al., 2013) and are accessible from NCBI’s Gene Expression Omnibus (access number: GSE41293). For sample Clustering and heatmap, read counts data were first transferred to homoscedastic data using a variance stabilizing transformation function in the DEseq package (Anders and Huber, 2010). Hierarchical clustering of the expression profile was generated by heatmap.2 of gplot package in R. For functional annotation analyses, pathways and gene network analyses were performed by IPA (Ingenuity Pathways Analysis, http://www.ingenuity.com/) with default parameters.

Copy number variation detection using whole genome sequencing (CNV-seq)

Analysis of somatic copy number variation using Illumina's next generation sequencing (CNV-seq) has been previously described by us and others (Daines et al., 2009; Venkatraman and Olshen, 2007). Illumina paired-end whole genome shotgun (WGS) libraries were prepared from 1 μg of genomic DNA extracted from four tumors and one

non-tumor tail sample from cNICD mice (matched genotype) as previously described (Daines et al., 2009) (Xie and Tammi, 2009). The resulting libraries were sequenced on the HiSeq 2000 platform using a paired-end 100bp sequence chemistry according to the manufacturer's instructions. Image analysis, base-calling and error calibration were performed using v1.4.0, v1.5.0 and v.1.8.0 of Illumina's Genome analysis pipeline. Alignment to the mouse reference genome version mm9 was performed using BWA (Li and Durbin, 2009). Bioinformatic identification of copy number variation (CNV) using Illumina next generation sequencing (CNV-seq) has been previously described by us (Daines et al., 2009) and others (Venkatraman and Olshen, 2007). The WGS data were scanned briefly by a variable size window in order to find regions of consistent coverage. These regions were then represented by their genomic midpoint positions and copy numbers. Further comparison between tumor and control samples determined a log2 coverage ratio for all analyzed regions. Those regions were then determined to be either gains or losses with the algorithm previously described (van de Wiel et al., 2007). Raw data from whole genome shotgun sequencing of Notch-induced tumors have been deposited into NCBI SRA database (accession number: SRP036865).

Cytogenetic region enrichment analysis

Cytogenetic region enrichment analysis (CREA) was performed as previously described, and a complete list of human genes for each chromosomal region can be found in the study by Walkley et al (Walkley et al., 2008). GSEA was performed using gene expression data obtained from the comparisons of primary NOS versus control bone tissues.

SUPPLEMENTAL REFERENCES

Anders, S., and Huber, W. (2010). Differential expression analysis for sequence count data. Genome Biol *11*, R106.

Daines, B., Wang, H., Wang, L., Li, Y., Han, Y., Emmert, D., Gelbart, W., Wang, X., Li, W., Gibbs, R., and Chen, R. (2011). The Drosophila melanogaster transcriptome by paired-end RNA sequencing. Genome research *21*, 315-324.

Gentleman, R., Carey, V., Bates, D., Bolstad, B., Dettling, M., Dudoit, S., Ellis, B., Gautier, L., Ge, Y., Gentry, J.*, et al.* (2004). Bioconductor: open software development for computational biology and bioinformatics. In, p. R80.

Ihaka, R., and Gentleman, R. (1996). R: A Language for Data Analysis and Graphics. Journal of Computational and Graphical Statistics *5*, 299-314.

Langmead, B., Trapnell, C., Pop, M., and Salzberg, S. L. (2009). Ultrafast and memory-efficient alignment of short DNA sequences to the human genome. Genome biology *10*, R25.

Lau, C. C., Harris, C. P., Lu, X. Y., Perlaky, L., Gogineni, S., Chintagumpala, M., Hicks, J., Johnson, M. E., Davino, N. A., Huvos, A. G.*, et al.* (2004). Frequent amplification and rearrangement of chromosomal bands 6p12-p21 and 17p11.2 in osteosarcoma. Genes, chromosomes & cancer *39*, 11-21.

Li, H., and Durbin, R. (2009). Fast and accurate short read alignment with Burrows-Wheeler transform. Bioinformatics (Oxford, England) *25*, 1754-1760.

Ma, O., Cai, W. W., Zender, L., Dayaram, T., Shen, J., Herron, A. J., Lowe, S. W., Man, T. K., Lau, C. C., and Donehower, L. A. (2009). MMP13, Birc2 (cIAP1), and Birc3 (cIAP2), amplified on chromosome 9, collaborate with p53 deficiency in mouse osteosarcoma progression. Cancer research *69*, 2559-2567.

Parkhomchuk, D., Borodina, T., Amstislavskiy, V., Banaru, M., Hallen, L., Krobitsch, S., Lehrach, H., and Soldatov, A. (2009). Transcriptome analysis by strand-specific sequencing of complementary DNA. Nucleic acids research *37*, e123.

Trapnell, C., Pachter, L., and Salzberg, S. L. (2009). TopHat: discovering splice junctions with RNA-Seq. Bioinformatics (Oxford, England) *25*, 1105-1111.

Trapnell, C., Roberts, A., Goff, L., Pertea, G., Kim, D., Kelley, D. R., Pimentel, H., Salzberg, S. L., Rinn, J. L., and Pachter, L. (2012). Differential gene and transcript expression analysis of RNA-seq experiments with TopHat and Cufflinks. Nat Protoc *7*, 562-578.

van de Wiel, M. A., Kim, K. I., Vosse, S. J., van Wieringen, W. N., Wilting, S. M., and Ylstra, B. (2007). CGHcall: calling aberrations for array CGH tumor profiles. Bioinformatics (Oxford, England) *23*, 892-894.

Venkatraman, E. S., and Olshen, A. B. (2007). A faster circular binary segmentation algorithm for the analysis of array CGH data. Bioinformatics (Oxford, England) *23*, 657-663.

Xie, C., and Tammi, M. T. (2009). CNV-seq, a new method to detect copy number variation using high-throughput sequencing. BMC bioinformatics *10*, 80.